arktos (2020) 6:75–92
https://doi.org/10.1007/s41063-020-00077-w

ORIGINAL ARTICLE

Late Quaternary sedimentation dynamics in the Beenchime-Salaatinsky Crater, Northern Yakutia

Georg Schwamborn[1,2] · Christoph Manthey[3] · Bernhard Diekmann[1] · Ulli Raschke[4] · Anatoly Zhuravlev[5] · Andrei V. Prokopiev[5] · Lutz Schirrmeister[1]

Received: 21 January 2020 / Accepted: 7 July 2020 / Published online: 28 July 2020

Abstract

The Beenchime-Salaatinsky Crater (BSC) is located west of the Olenyok River in Northern Yakutia, ~ 260 km south-west of Tiksi and the Lena Delta. The age and origin (volcanic versus meteoritic) of this crater is poorly understood. The key scientific interest in re-visiting the BSC is the reappraisal of the Quaternary sedimentation dynamics for a better understanding of the sediment history and thickness in the basin. This aides for an assessment, if the site is prospective for a deeper drilling of a Quaternary (or Cenozoic) sediment archive. Soil pits and auger cores from slopes and lowland terrain in the basin were sampled and studied to infer sediment ages and transport dynamics. This also included a thermokarst lake placed in the centre of the basin. Studied properties include grain-size distribution, organic carbon and nitrogen contents (TOC and TN), heavy mineral compositions, $\delta^{13}C$ of organic carbon, ^{14}C ages from sediment, $\delta^{18}O$ and δD from ground ice and waters, and lake bathymetry from GPR profiling, in addition. We conclude that the crater floor in the BSC is underlain by fluvial/alluvial sediments from the MIS 3 period. Thermokarst lake formation took place during the Holocene Thermal Maximum between 7600 and 6100 cal yr BP. The lake has been shrinking hereafter. Fluvial/alluvial sedimentation along the drainage pattern was active again between 5700 to 1500 cal yr BP, and it was flanked by the accumulation of peaty and organic-rich sediments and the formation of ice-wedge polygons.

Keywords Quaternary · Permafrost · Impact structure · Northern Siberia

Introduction

A geologic and geophysical sampling project in northern Yakutia is designed for tracing back Arctic permafrost inception and Cenozoic environmental changes on a yet unknown time scale—potentially several million years. The locality is the Beenchime-Salaatinsky Crater (BSC) in northern Yakutia, which presumably arose around 40 million years ago and has been acting as a sediment trap for a yet unknown period. If the given ages are true, the BSC may contain the oldest environmental archive of the terrestrial Arctic. A multimillion-year old continental record from the BSC could become a counterpart to the prominent marine ACEX core, which was collected over the North Pole and stretches back to the Palaeocene/Eocene (ca. 55 million years ago, [36]). If the core consists of lake sediments to a great part, it possibly can be compared with the palaeoclimate and palaeoenvironmental history contained in the 3.5 million years old record from El'gygytgyn Impact Crater Lake [10, 30]. In any case,

✉ Georg Schwamborn
gschwamborn@gmail.com

1 Alfred Wegener Institute Helmholtz Centre for Polar and Marine Research, Telegrafenberg A45, 14473 Potsdam, Germany

2 Eurasia Institute of Earth Sciences, Istanbul Technical University, Maslak, Istanbul 34469, Turkey

3 Institut für Geowissenschaften, Universität Potsdam, Karl-Liebknecht-Street 24–25, 14476 Potsdam, Germany

4 Bundesanstalt für Geowissenschaften Und Rohstoffe (BGR), Geozentrum Hannover, Stilleweg 2, 30655 Hannover, Germany

5 Diamond and Precious Metal Geology Institute, Russian Academy of Sciences, Siberian Branch, Prospekt Lenina, 39, 677000 Yakutsk, Russia

a long BSC environmental record at least can serve for studying periglacial and permafrost processes on a Quaternary time scale in an area that today has an estimated permafrost thickness of > 500 m [13]. Even though BSC has been a closed basin for a long time, a multidisciplinary research would benefit from analysing a big variety of scientific fields such as sedimentology and permafrost hydrology, geomorphology, near surface, and borehole geophysics. The study scope would also include mineralogy, geochemistry, and isotope analyses along with studying vegetation diversity, macrofossil (e.g., ostracods, diatoms, and gastropods) and microbial diversity, biomarker detection, and drilling technology.

Little is known about the beginning of permafrost formation and the associated environmental and climate conditions, this may help to better interpret long-term permafrost dynamics. It is suspected that permafrost had its origin at the beginning of the Pleistocene era 2.6 million years ago, but this should not imply that more ancient and intervening thermal conditions were without significance [27]. The late Pleistocene environment of North Yakutia favoured accumulation of ground ice and formation of syngenetic permafrost. Severely cold climate and polygenetic sedimentation (i.e., aeolian, fluvial, alluvial, and nival processes) resulted in building up frozen sediment sequences that are several dozens of meters thick [47, 49, 54]. In fact, extremely ice-rich and silt-dominated permafrost deposits (termed "Yedoma Ice Complex") were formed and remain one of the most prominent features of the periglacial environment in the terrestrial Arctic. The dry and cold conditions over much of the Pleistocene in Northeast Siberia [19] ensured that depositional basins in the region have remained ice free, which thus may have accumulated a near continuous record of environmental and climate proxies in this area. An enclosed basin such as the BSC allows for studying a variety of multiproxy data (biotic and mineralogic indicators) to reconstructing the environmental conditions framing the permafrost evolution in the area.

Various detailed palaeoenvironmental reconstructions have been made from frozen depositional sequences including Yedoma Ice Complex and they cover a time axis back to marine isotope stage (MIS) 6 [60]. Understanding the nature and distribution of ice-rich permafrost is of concern, because it is widespread in Arctic and sub-Arctic east Siberia, and it provides the foundation for diverse Arctic and boreal ecosystems that are exposed to permafrost thawing, if permafrost warming continues [8].

The BSC, located west of the Olenyok River in Northern Yakutia (Fig. 1), is an 8-km-wide basin inside a ring structure that has neither been verified for its Quaternary sediment age and thickness, nor for its potential to allow a palaeoenvironmental reconstruction in the area, and it is placed in a corridor that has never been glaciated

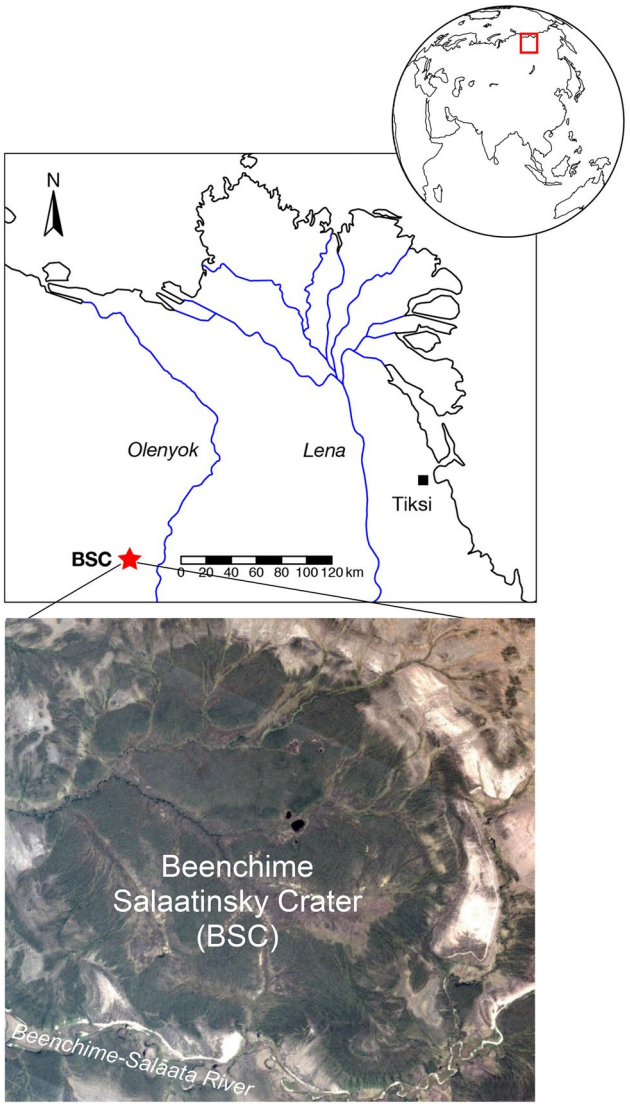

Fig. 1 Schematic map with inset and satellite view of the study region (credits: PlanetScope [40], I. Nitze under "Personal Research License"). The red star marks the location of the BSC (Beenchime-Salaatinsky Crater). The circular shape, which has 8 km in diameter, as seen on satellite imagery

during the Pleistocene [15]. It has been a prospective site, although the crater is virtually unknown in terms of its age. A multi-million-year old formation is likely due to its geomorphological down worn crater rim, the BSC is listed as 65 M years old [35], < 65 M years old [18], or 40 ± 20 M years old (data from [14]). The formation of the crater has been debated differently. Pinchuk [43] and Khain [23] describe the BSC as a kimberlitic pipe of uncommon size, comparable to the kimberlitic pipe Mwadui in Tanzania, whereas Mikhailov et al. [34] and Masaitis [29] preferred a formation due to a meteoritic impact event.

Scientific key interests for re-visiting BSC were (i) assessing sediment processes and ages of the Quaternary

strata and (ii) determining the potential of the basin to preserve a long-lasting Quaternary sedimentary archive. Field work focused on sampling of near-surface deposits from frozen ground (down to 2 m depth) and from a shallow thermokarst lake (water depth 5 m at maximum), which is placed in the crater's centre.

Study site

BSC is placed in the north-eastern part of the Siberian Craton ([29], Fig. 1) and named after the nearby passing rivers Beenchime (south) and Salaata (west). Formed by collisions of several microcontinents of different ages, the basement of the Siberian Craton consists of Lower Precambrian rocks (cropping out primarily in the Anabar and Aldan shields). In the study area, the crystalline bedrock is overlain by Upper Precambrian and Lower-to-Middle Cambrian platform sediments including carbon-bearing formations and argillocarbonates [26, 44]. Next to this, marine sedimentary rocks of Upper Cambrian-to-Lower Triassic age are described for this area [26].

The geology of the crater is dominated by Cambrian limestones and dolomites partially mixed with siliceous sandstones, conglomerates, and Permian sandstones [39]. To the north and south-west of the BSC, Upper Palaeozoic allogenic breccia has been identified.

BSC forms a circular basin with a fairly gentle topographic relief partially filled by Quaternary sediments dipping slightly to the west [34]. The inner part has a seasonally active drainage pattern exiting the crater rim to the west. A second break of the rim is located in the southern segment of the rim (Fig. 2).

Based on literature data, the following scenario is summarised with respect to the BSC basin history: (i) platform sedimentation during Vendian, Cambrian, and Permian time [39], (ii) (Post-) Permian impact event, Mesozoic (Lower Triassic) overburdening [26], (iii) subsequent erosion in the course of the Mesozoic–Cenozoic Olenyok Uplift [26] with exposure, erosion, and mobilisation of Paleozoic rock.

Inside the crater, the distribution of Quaternary sediments can be attributed to two morphological levels; the lower one (Holocene) is dominated by the seasonally active river network and holds polygonal patterned ground. Partly, this area is subaerially degrading, and partly, it is boggy. It is vegetated by forest tundra and shrubs. The upper level (late Pleistocene to Holocene) lacks those physiographic features and is covered by forested tundra with Larix stands (Fig. 2).

The area has sub-Arctic climate. Data from the closest weather station in Olenek (241,250, N68.5000, E112.4331) provided by NOAA show an average annual precipitation of 285 mm and an average temperature of −12.4 °C with a maximum of 20.3 °C and a minimum of −42.7 °C (period: 1961–1990).

Materials and methods

Field work

During fieldwork in July 2016 [50], six sites from the basin lowland have been sampled (Fig. 2). Sample depths ranged between 0.80 m and 1.85 m. Samples were collected by digging the active layer and drilling into the upper permafrost using an SIPRE Coring Auger Set (diameter 70 mm). Three sections are located on polygonal patterned ground in the central part (BSC-PS-02, BSC-PS-05A, BSC-PS-05B). Others (BSC-PS-01, BSC-PS-03, and BSC-PS-04) are located in areas, which are interpreted to be remains of ancient fluvial terraces. BSC-PS-02 is located in the centre of a degrading polygon. BSC-PS-05A and BSC-PS-05B are located in a low-centre polygon near the shoreline of the biggest lake in the crater's centre (informally named "Big Lake"; labels A and B result from relocating the equipment at close distance of 50 cm. Sediment field description included colour, grain-size composition, occurrence of organic material, and ground ice fabric. Gravimetric ice contents were measured already in the field and are expressed as weight percentage (wt%). For comparison with sediment and ground ice properties, we also sampled lake water from the Big Lake (BSC-W) and water and surface sediment from the nearby Beenchime-Salaatinsky River (BSC-FS).

Three short cores have been collected from the Big Lake. The cores had lengths of 0.22 m, 0.30 m, and 0.51 m, and were extracted using a UWITEC gravity corer. One of them is further analysed for this study (BSC-LS-03). Information on bathymetry and lake bed geomorphology was acquired with a 50 MHz GPR antenna (ground-penetrating radar from Mala/Geoscience). GPR profiling was conducted from a rubber boat along two traverse lines running perpendicular to each other (Fig. 3). The water depth has been repeatedly verified by manual measurements using a rope with a weight fixed to it. GPR data were recorded in the single-offset mode with a GPS receiver connected to the system. Good penetration of the electromagnetic waves was permitted through the water column, since the lake water has a low conductivity (~ 160 µS/cm). The data were imported into standard processing software (ReflexW) and an optimal processing flow determined included the following standard procedures: (i) subtract DC shift, (ii) static correction, (iii) bandpass lower 12.5 MHz, upper 70 MHz, (iv) auto interpolation, and (v) travel time-to-depth conversion with a depth axis $v = 0.033$ m/ns for water [51].

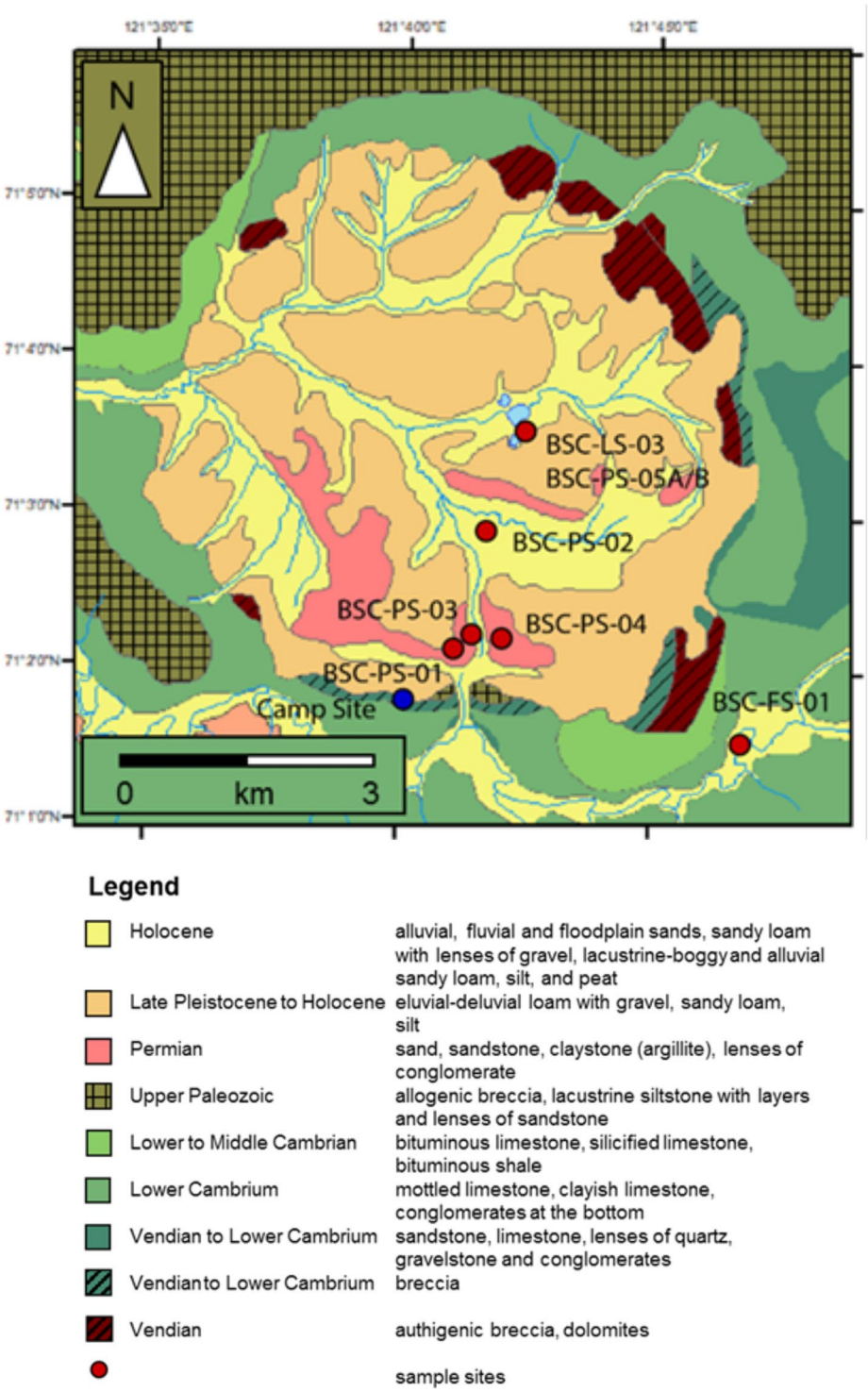

Fig. 2 Geological map of the Beenchime-Salaatinsky Crater with field sites (modified from [39])

Laboratory work

After transport to the lab, the sediment samples were analysed for the following properties. Mass-specific magnetic susceptibility (MS) was measured on freeze-dried subsamples with a Bartington MS2 magnetic susceptibility system using the low-frequency option of a MS2B Sensor. The data are expressed in SI units (according to Le Système International d'Unités, 10^{-8} m^3 kg^{-1}). For analysing grain-size distribution (GSD), a Malvern Mastersizer 3000 was used. For total carbon (TC) and total nitrogen (TN) content, samples were measured on a Vario EL III element analyser with reference to three lab internal standards (IVA 2150, STSD-4, and GSD-4). Total organic carbon

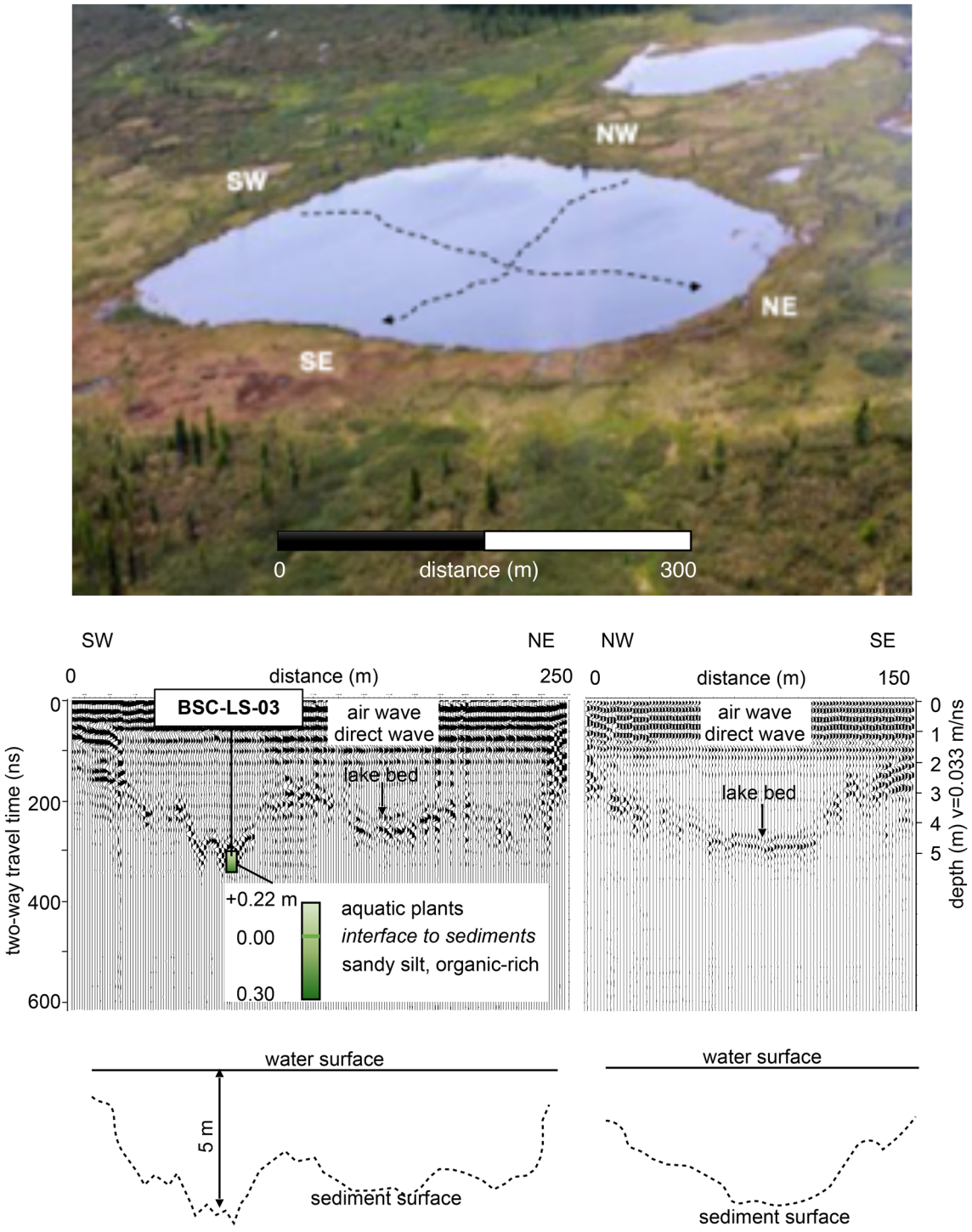

Fig. 3 Oblique view of the Big Lake with the approximated positions of GPR lines added (top). Two GPR profiles recorded perpendicular to each other. Basic interpretations are given in and below radargrams. The arrow indicates the location where lake sediments have been sampled (BSC-LS-03). Depth axis (m) accounts for electromagnetic velocity in water

(TOC) content was measured on a VarioMax C using glutamine–quartz mixtures of different ratios as references. Values for inorganic carbon (TIC) were calculated by subtracting TOC from TC. The composition of stable organic carbon isotopes ($\delta^{13}C$) was analysed on a Thermo Fisher Delta V Advantage mass spectrometer with USGS24 tryptone and polyethylene as standards. For the analysis of heavy mineral (HM) composition, selected samples were

separated by density solution after the 63–125 µm fraction was extracted by sieving. For inspections under the microscope, particles were attached on slides with Meltmount 1.68™ and around 200 grains were counted following procedures outlined in Boenigk [9]. In addition, material found in Mange and Maurer [28] was used as reference for identification. Radiocarbon dating was done by MICADAS (MIni radioCArbon DAting System, AWI Bremerhaven) and by CologneAMS (University of Cologne). For calibration of ^{14}C ages into calendar years, the routine of Stuiver et al. [56] was performed using the IntCal13-curve and the CALIB 7.1 Internet program.

Analysis of pH and electrical conductivity (EC) from ground ice and water samples was done already in the field with a WTW system using pH-Electrode Sentix 81 and TetraCon 325. Stable water isotopic composition (δD, $\delta^{18}O$) was measured on a Finnigan MAT Delta-S mass spectrometer. The values are given as per mil (δ, ‰) difference from the Vienna Standard Mean Ocean Water (VSMOW) standard, with internal 1σ errors of better than 0.8‰ for δD and 0.1‰ for $\delta^{18}O$. The deuterium excess (*d*-excess) is calculated according to Dansgaard [11] as $d = \delta D - 8\delta^{18}O$.

Results

Radiocarbon ages

When grouping the samples according to their ages (Fig. 4; Table 1), it becomes obvious that sediments filling the crater lowland have been deposited during the late Pleistocene Kargin Interstadial (~MIS 3, [59]) and during the Holocene (~MIS 1). Kargin sediments are found in sections BSC-PS-01, -03, and -04, whereas Holocene deposits are associated with organic-rich and peaty sections of BSC-PS-02 and -05 and lake sediments from core BSC-LS-03 (Fig. 5).

The material used for radiocarbon dating is different in nature. Sites BSC-PS-01, -03, and -04 are dominated by sandy to silty sediments and dating of these sections mostly relies on bulk detritus. BSC-PS-03 and -04 allowed for only one date in each of the sections (Table 1) in the absence of other datable material. BSC-PS-01 has late Pleistocene deposits overlain by late Holocene sediments. BSC-PS-03 and -04 layers point to a late Pleistocene age in the absence of more datable material, whereby BSC-PS-03 provided only an individual piece of charcoal for dating. In contrast, peaty sections BSC-PS-02 and -05 allowed for picking rootlets and wood fragments (Table 1) and lake sediments from short core BSC-LS-03 are rich in macroscopic plant remains and organic detritus. This allowed for a better temporal resolution of the peaty and lake sediments when compared with the soil pit deposits mentioned above. Age inversions occur in all studied depositional settings; in sandy sediments

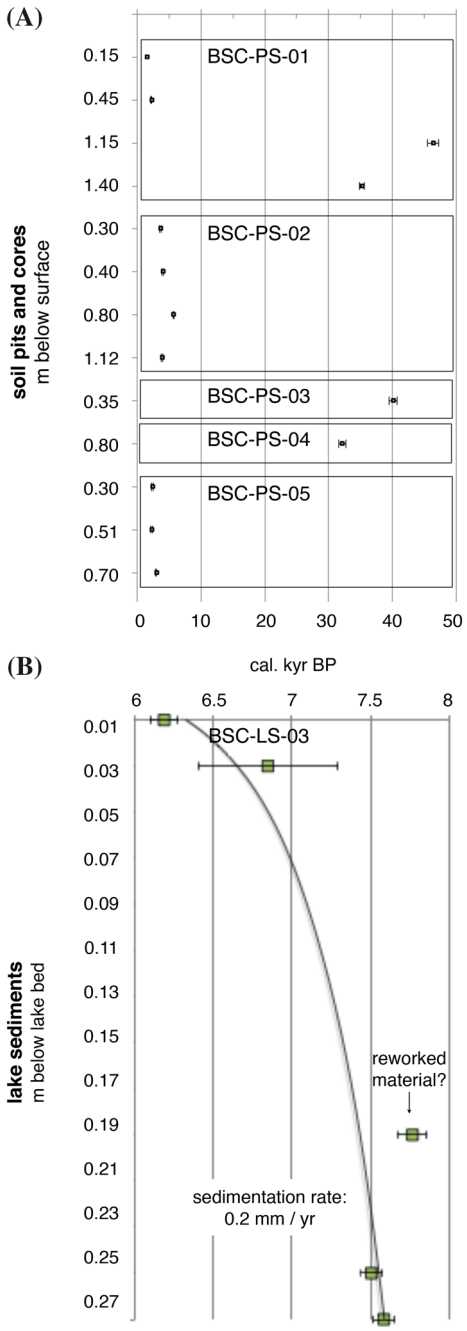

Fig. 4 Calibrated ^{14}C ages with 2-sigma error bars based on CALIB 7.1: (**a**) for samples from soil pits; (**b**) for lake sediments

(BSC-PS-01), in the peaty section (BSC-PS-05), and in the lake sediments (BSC-LS-03).

Bathymetry

Below first arrivals of air wave and direct wave, the GPR profiles image the first subsurface reflector below shallow water in the Big Lake (Fig. 3). The reflector plunges fairly

Table 1 List of dated samples

Sample	Depth (m)	^{14}C age (year BP)	±	Cal yr BP (2σ)	Type	Lab ID
BSC-PS-01-03	0.15–0.20	1660	47	1475–1634	Bulk	AWI1411.1.1
BSC-PS-01-05B	0.45–0.50	2249	36	2154–2273	Bulk	COL4272.1.1
BSC-PS-01-05B	0.45–0.50	Modern		–	Rootlets	COL4271.1.1
BSC-PS-01-10	1.15–1.30	43,086	413	45,446–47,202	Bulk	COL4273.1.1
BSC-PS-01-13	1.40–1.60	31,326	142	34,828–35,579	Bulk	AWI1412.1.1
BSC-PS-02-03	0.30–0.34	3437	50	3583–3831	Plant remains	AWI1476.1.1
BSC-PS-02-05	0.40–0.50	3681	51	3877–4151	Plant remains	AWI1281.2.1
BSC-PS-02-12	1.12–1.20	3588	51	3811–3994	Plant remains	AWI1282.2.1
BSC-PS-02-21	0.80–0.85	4974	40	5604–5754	Plant remains	COL4274.1.1
BSC-PS-03-04B	0.35–0.45	35,475	236	39,470–40,688	Charcoal	COL4275.1.1
BSC-PS-04-05B	0.80–0.85	28,247	139	31,575–32,655	Bulk	COL4276.1.1
BSC-PS-04-05B	0.80–0.85	46,514	640	-	Charcoal	COL4277.1.1
BSC-PS-05A-04	0.30–0.41	2383	50	2327–2540	Plant remains	AWI1284.2.1
BSC-PS-05A-06	0.51–0.60	2296	50	2152–2380	Plant remains	AWI1285.2.1
BSC-PS-05B-02	0.03–0.40	71	48	–	Plant remains	AWI1477.1.1
BSC-PS-05B-06	0.70–0.80	2873	49	2870–3083	Plant remains	AWI1478.1.1
BSC-LS-03-12	0.22–0.24	5369	49	6096–6280	Plant remains	AWI1413.1.1
BSC-LS-03-13	0.24–0.26	5991	198	6401–7293	Wood fragments	AWI1071.1.2
BSC-LS-03-21	0.40–0.42	6928	49	7669–7859	Bulk	AWI1414.1.1
BSC-LS-03-25	0.47–0.49	6619	49	7434–7573	Bulk	AWI1415.1.1
BSC-LS-03-26	0.49–0.51	6710	43	7505–7659	Bulk	COL4270.1.1

Calibration according to IntCal [56]

steeply towards the central lake part. It undulates in both profiles with greater vertical differences in the longer profile (up to 2 m, left panel), and a more bowl-shaped curve in the shorter profile (right panel). Towards the SE end of the shorter profile, there is rugged subaquatic morphology. A similar topography is also indicated in the SW–NE profile. This first subaquatic reflector is interpreted to represent the lake bed. According to the travel time-to-depth conversion the water depth is greatest at about 5 m as can be seen in the SW-NE profile. Below the first reflector, the energy is quickly absorbed and any more subground information is masked.

Cryolithology and sedimentology

Soil pits

Section BSC-PS-01 belongs to an ancient sediment terrace partly covering the crater floor. It has been sampled down to 1.6 m depth with the permafrost table at 1.0 m depth (late July 2016, Figs. 2, 5). Sediments are composed of sand or sand-dominated units including an organic-rich layer between 0.2 and 0.15 m depth. The ground ice content decreases from 43 wt% to 16 wt% between 1.50 m and 1.08 m. At the permafrost table, lenticular ice lenses of several centimetres thickness can be observed. The ground ice stable isotopes range between −23.25‰ and −19.94‰ (δ^{18}O) and −168.83‰ to −152.01‰ (δD) with values becoming heavier to the top. The *d*-excess decreases from 17.7 to 7.5 (Table 3). Sediments become finer from the bottom to the top (Fig. 5) and show prominent peaks in their grain-size composition in the fine sand and in the fine silt spectrum (Fig. 6). The profile is dated at depths of 1.5 m (35,190 cal yr BP), 1.23 m (46,265 cal yr BP), 0.48 m (2234 cal yr BP), and 0.18 m (1564 cal yr BP) (Fig. 5). From a sample depth 0.50–0.45 m, a root fragment is dated as modern. MS values have little variation between 13 and 18 SI. TOC and TN values are overall low. Highest values occur in the top 0.6 m with TOC up to 4.1% and TN up to 1.9%. TIC is low between 0% and 0.8%. The TOC/TN ratio ranges between 7.6 and 21.5. The δ^{13}C values decrease upward from −23.99‰ to −28.94‰. The HM composition from BSC-PS-01-, 02, and -12 is dominated by opaque minerals (~ 67%), followed by garnet (~ 17–19%) and zircon (~ 5%) (Table 2).

BSC-PS-03, drilled in the same terrace as BSC-PS-01, was sampled down to 1.1 m depth, is made of sand and contains patches of dark, organic-rich material between 0.5 and 0.26 m depth. The sandy sediments peak in the fine-sand spectrum (Fig. 6). At a depth of 0.40 m, sediments were dated to an age of 40,067 cal yr BP. The MS shows little variation with overall low values between 9 and 24 SI similar to BSC-PS-01 (Fig. 5). The ice content from just below the permafrost table at 1.0 m amounts to 19 wt%.

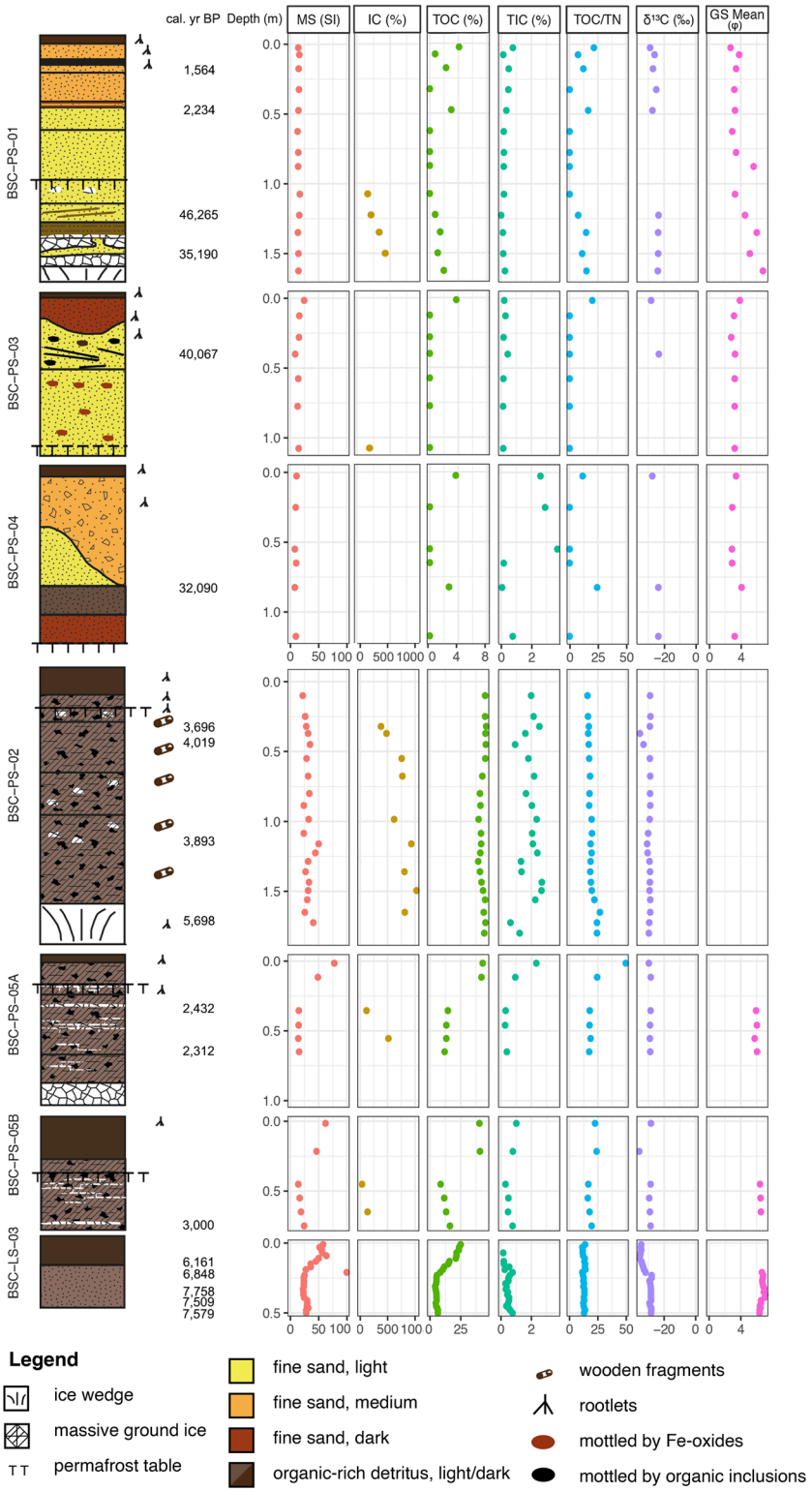

Fig. 5 Sediment sections and measured properties including MS, IC (ice contents), TOC, TIC, TOC/TN, $\delta^{13}C$, and grain-size composition (GS). Note changes in the TOC scale

With no excess ground ice present, stable water isotope measurements were discarded for this profile. The TOC and TN contents are overall low, partly below the detection limit, and have their highest values at the section top with 3.7% (TOC) and 0.19% (TN). Also, TIC values are low with low variation and a maximum of 0.44% at 0.4 m depth. $\delta^{13}C$ could be extracted from two samples from a depth of 0.40 m (−23.27‰) and from the surface (−28.27‰). HM compositions (Table 2) are dominated by opaque minerals (62%), followed by garnet (17%), zircon (6%), and epidote minerals

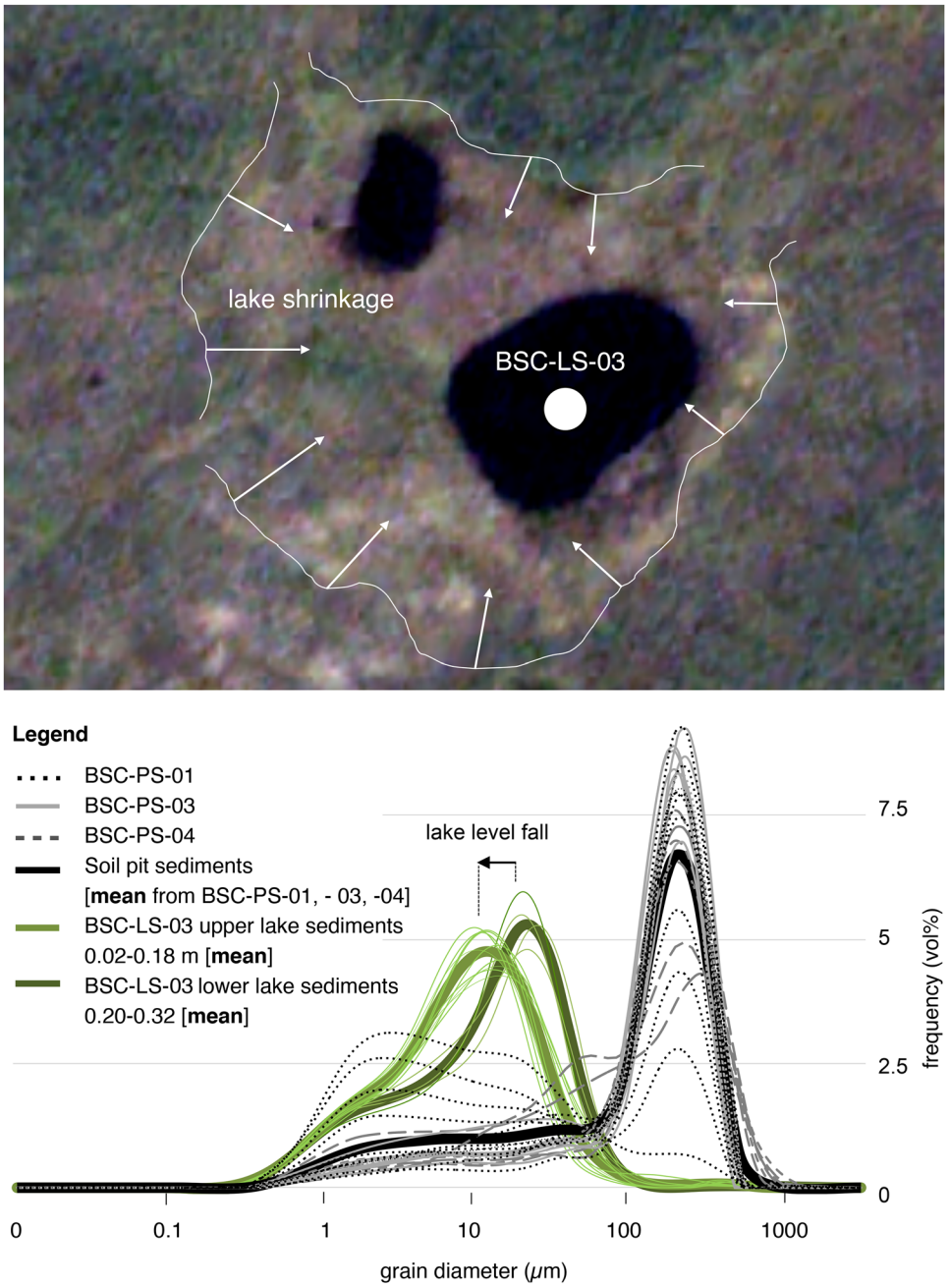

Fig. 6 Frequency of mean grain sizes of soil pit sediments (interpreted fluvial/alluvial) and lake sediments. Lower lake sediments (BSC-LS-03) are coarser than upper lake sediments. Arrows in satellite image mark lake area shrinkage (credits: PlanetScope [40], I. Nitze under "Personal Research License")

(7%, i.e., epidote, zoisite, and clino-zoisite). For comparison, the sample taken from Beenchime-Salaatinsky River (BSC-FS) has a bimodal grain-size composition with peaks for medium sand and medium silt. MS is low (10 SI), TOC, and TN are negligible. HM composition is dominated by opaque minerals (41%) with higher portions of pyroxenes (15%), amphiboles (20%), and epidote minerals (9%) (Table 2).

BSC-PS-04 belongs to the same ancient fluvial terrace as BSC-PS-01 and BSC-PS-03, and is located 350 m east of BSC-PS-03 on the opposite side of a boggy valley. The core, sampled down to 1.2 m depth, consists of a sand with fine gravel admixed and silt lying discordantly (0.80–0.40 m) on top of a fine-sand layer. The grain-size distribution peaks in the medium and very fine-sand spectrum (Fig. 6). Excess ground ice was absent and stable water isotope measurements were discarded for this profile. Samples from 0.83 m depth were dated to 32,090 cal yr BP using the bulk fraction and to 46,513 ± 640 year BP (uncalibrated) using a charcoal fragment (Table 1). MS values show little variation around 9 SI (Fig. 5). TN values are close to the detection limit, except at a depth of 0.82 m (0.1%) and at the surface (0.3%). Similarly, TOC values are often below the detection limit but peak to 2.7% at 0.82 m depth and 3.6% at the surface. TIC is low below 0.60 m depth (below 0.8%) and higher

Table 2 Heavy mineral fractions in BSC sediment samples (grain %)

Sample	BSC-PS-01–02	BSC-PS-01–12	BSC-PS-03–02	BSC-PS-03–07	BSC-PS-04–02	BSC-PS-04–06	BSC-FS-01
Opaque	67	68	64	62	48	69	41
Garnet	19	18	13	21	18	16	3
Zircon	6	5	6	5	16	5	5
Rutile	1	0	1	0	3	2	1
Tourmaline	1	0	0	0	0	0	0
Epidote	1	2	5	2	5	3	9
Zoisite	1	0	2	2	4	1	5
Clinozoisite	0	1	1	1	1	1	2
Orthopyroxene	1	1	0	0	0	1	9
Clinopyroxene	0	0	0	0	2	0	6
Hornblende	1	0	2	1	1	0	20
Amphibole	0	0	0	0	0	0	1
Apatite	2	3	3	3	1	3	1
Biotite	0	0	0	0	0	1	0
Sphene	0	2	2	1	0	0	0
Disthene	0	0	0	0	0	0	0
Sillimanite	0	0	0	0	0	0	0

Table 3 Electrical conductivity (EC), pH, and stable water isotope composition of BSC samples

Sample	Depth (m)	EC (µS/cm)	pH	$\delta^{18}O$ (‰) vs. SMOW	1σ	δD (‰) vs. SMOW	1σ	*d*-excess	Note
BSC-W-01	3.50–4.20	162	8.9	− 19.0	0.0	− 146.7	0.3	5.0	Lake
BSC-W-02	2.30–3.00	82	9.5	− 18.9	0.0	− 146.5	0.3	5.1	Lake
BSC-W-03	0.30–1.00	101	9.3	− 18.9	0.0	− 146.5	0.3	5.0	Lake
BSC-W-04	0.00–0.10	79	9.2	− 17.9	0.0	− 138.7	0.2	4.5	River
BSC-PS-01-10	1.15–1.30	795	7.5	− 19.9	0.0	− 152.0	0.3	7.5	Pore Ice
BSC-PS-01-11	1.30–1.40	526	7.2	− 20.2	0.0	− 153.8	0.4	7.7	Ice lense
BSC-PS-01-12	1.40–1.60	2168	7.0	− 22.2	0.0	− 163.8	0.3	14.0	Ice vein
BSC-PS-01-13	1.60–1.65	399	8.0	− 23.3	0.0	− 168.3	0.4	17.7	Ice wedge
BSC-PS-02-05	0.40–0.50	171	6.9	− 18.4	0.0	− 138.2	0.2	8.9	Pore ice
BSC-PS-02-10	0.92–1.05	215	6.7	− 19.2	0.0	− 145.9	0.2	7.3	Ice lense
BSC-PS-02-14	1.25–1.32	203	7.5	− 19.2	0.0	− 145.5	0.3	7.8	Pore ice
BSC-PS-02-17	1.47–1.52	128	7.3	− 19.1	0.0	− 145.0	0.2	7.6	Pore ice
BSC-PS-02-18	1.52–1.60	152	7.0	− 19.1	0.0	− 145.0	0.4	7.9	Pore ice
BSC-PS-02-19	1.60–1.70	111	6.8	− 19.0	0.0	− 144.0	0.4	8.1	Pore ice
BSC-PS-02-20	1.70–1.80	44	6.8	− 18.5	0.0	− 141.0	0.2	7.3	Ice vein
BSC-PS-02-21	1.75–1.85	19	6.8	− 17.3	0.0	− 133.1	0.4	5.6	Ice vein
BSC-PS-05A-04	0.30–0.41	36	5.5	− 18.4	0.0	− 139.1	0.3	7.8	Ice vein
BSC-PS-05A-05	0.41–0.51	34	5.4	− 19.0	0.0	− 145.1	0.3	7.0	Ice vein
BSC-PS-05A-06	0.51–0.60	36	5.4	− 18.5	0.0	− 142.7	0.3	5.0	Pore ice
BSC-PS-05A-07	0.60–0.70	43	5.7	− 19.4	0.0	− 151.0	0.3	4.3	Pore ice
BSC-PS-05A-08	0.70–0.82	17	6.3	− 26.7	0.0	− 203.5	0.2	9.9	Ice wedge
BSC-PS-05A-09	0.82–0.90	15	6.3	− 26.2	0.0	− 200.3	0.3	9.0	Ice wedge
BSC-PS-05A-10	0.90–0.95	24	6.7	− 26.6	0.0	− 202.1	0.3	10.8	Ice wedge
BSC-PS-05A-11	0.95–1.05	92	8.5	− 26.5	0.0	− 201.2	0.3	11.0	Ice wedge

in the upper profile part (> 2.6%). TOC/TN ratios increase from 11.6 at the profile bottom to 24.3 at the profile top. The $\delta^{13}C$ values become lighter upwards from −23.67‰ to −27.46‰. The HM composition is dominated by opaque minerals, which decrease from the bottom to the top from 69 to 47%. Subordinate heavy minerals are garnet, zircon, and epidotes (Table 2).

BSC-PS-02 has been drilled down to 1.8 m depth and is located within the seasonally active river network. It consists of ice-rich peat (pore ice and ice veins). The section is underlain by massive ground ice, which was visible at the core bottom. The mineral fraction of the organic deposits was negligible and a grain-size determination was discarded. The ground ice stable isotope composition is heavier than in BSC-PS-01, and $\delta^{18}O$ varies between −19.16‰ and −17.33‰ and δD between −145.93‰ and −133.05‰; the *d*-excess ranges between 5.6 and 8.9.

Dated samples have the following ages: 1.16 m (3893 cal yr BP), 0.45 m (4019 cal yr BP), and 0.32 m (3696 cal yr BP) (Table 1). A plant fragment found in the underlying massive ice was dated to 5689 cal yr BP. MS values decrease from 40 to 22 SI upward including a peak of 50 SI at 1.16 m depth (Fig. 5). The ice content decreases upwards from 89 wt% (1.65 m) to 79 wt% (0.32 m) with individual maxima of 91 wt% (1.50 m) and 89 wt% (0.67 m). TOC contents are high in the profile (40–46%). TN values slightly increase upwards from 1.8% to 2.4% and a maximum at 0.25 m depth (2.8%). TIC values are above 2% and reach almost 3% at depths of 1.56 m and 1.44 m. TOC/TN ratios are fairly constant around a maximum value of 26.7% at 1.65 m depth. $\delta^{13}C$ is ranging between −30.79 and −28.69‰ with a negative peak between 0.40 and 0.30 m depth (−35.45‰).

BSC-PS-05A/-05B, located at the southern margin of the Big Lake and sampled down to 1.0 m, is also dominated by peaty deposits. It has similar ground ice structures as seen in BSC-PS-02, and similarly, massive ground ice is underlying the sampled section. $\delta^{18}O$ varies between −26.68‰ and −18.36‰ and δD varies between −203.47‰ and −139.09‰, and has the lightest values at the bottom. Remarkably, all hydrochemical values from this section show a distinct offset occurring at 0.70 m depth when the massive ice is encountered, e.g., $\delta^{18}O$ becomes heavier by about 7‰ and δD for more than 50‰. This offset is also mirrored in the d-excess trend, which ranges between 11.0 and 4.3 (Table 3).

Samples of BSC-PS-05A have a minor portion of mineral content, which peak in the medium silt spectrum (Φ 5, Fig. 5). Radiocarbon dating reveals ages of 2312 cal yr BP (0.55 m depth) and 2432 cal yr BP (0.35 m depth) (Table 1). From the bottom to the top, MS increase from 14 to 78 SI and TOC is moderate at the bottom (12%) and high at the top (43%). TN contents increase from 0.7% to 0.9% with an individual maximum at 0.12 m (1.7%) and TIC contents increase from 0.4% to 2.3%. $\delta^{13}C$ ranges fairly constant around −29‰. The ice content accounts for 84 wt% (0.56 m) and 54 wt% (0.36 m). Section BSC-PS-05B, sampled in half a meter distance to BSC-PS-05A, overall has the same sediment characteristics as described above (Fig. 5).

Lake core

The lake sediments are composed of silty sediments rich in organic detritus. Remarkably, the lower lake sediments (0.52–0.44 m) are slightly coarser (mean mode at 25 µm) when compared with the overlying lake sediments (mean mode at 15 µm) and are shifted by 10 µm with their mean peak from the medium to the fine silt spectrum.

TOC values in the lake sediments increase from the bottom to the top from 4.2 to 25.1%. MS values increase from 28 to 58 SI including a distinct peak of 99.5 SI (0.21 m), where the boundary is between more consolidated sediment at the bottom and more loose sediment overlying them (Fig. 5). TN increases upwards from 0.5% to 1.8% and TIC decreases upwards from 0.8% to almost 0%. The TOC/TN ratio is relatively constant around 12. $\delta^{13}C$ become lighter from the bottom to the top from −28.26‰ to −34.46‰, where remains of modern aquatic plants concentrate. Radiocarbon dating has ages of 7579 cal yr BP (0.49 m), 7509 cal yr BP (0.47 m), 7758 cal yr BP (0.40 m) and 6848 cal yr BP (0.24 m), and 6161 cal yr BP (0.23 m) (Table 1). The fluffy organics floating over the lake floor are considered living aquatic plants that have not been dated. For completeness, they have been added to the sample column (LS-03, see Figs. 3, 5), since samples from the water plants have been used for $\delta^{13}C$ analysis (see below).

Organic source identification using TOC/TN and $\delta^{13}C$

Plotting TOC/TN versus $\delta^{13}C$ is used to illustrate the proportional mixing of terrestrial and subaquatic sedimentary organic matter according to Meyers [33]. The sandy sections (BSC-PS-01, -03, -04) group mostly in the transitional field between the two fields (Fig. 7a) with some individual samples indicating a pure origin from either "C3 land plants" or "lacustrine algae". Plotting the peat locations (BSC-PS-02, -05A/B) shows higher TOC values when compared with the sandy sections and $\delta^{13}C$ becomes distinctly lighter (Fig. 7b). Much of the samples from the two peaty sites group in the field "C3 land plants". Organic matter from the lake (BSC-LS-03) shows data points that all group in the transitional field between the two fields "lacustrine algae" and "C3 land plants". Samples with lightest $\delta^{13}C$ values (−32‰ to −36‰) are related to the unconsolidated fluffy organics

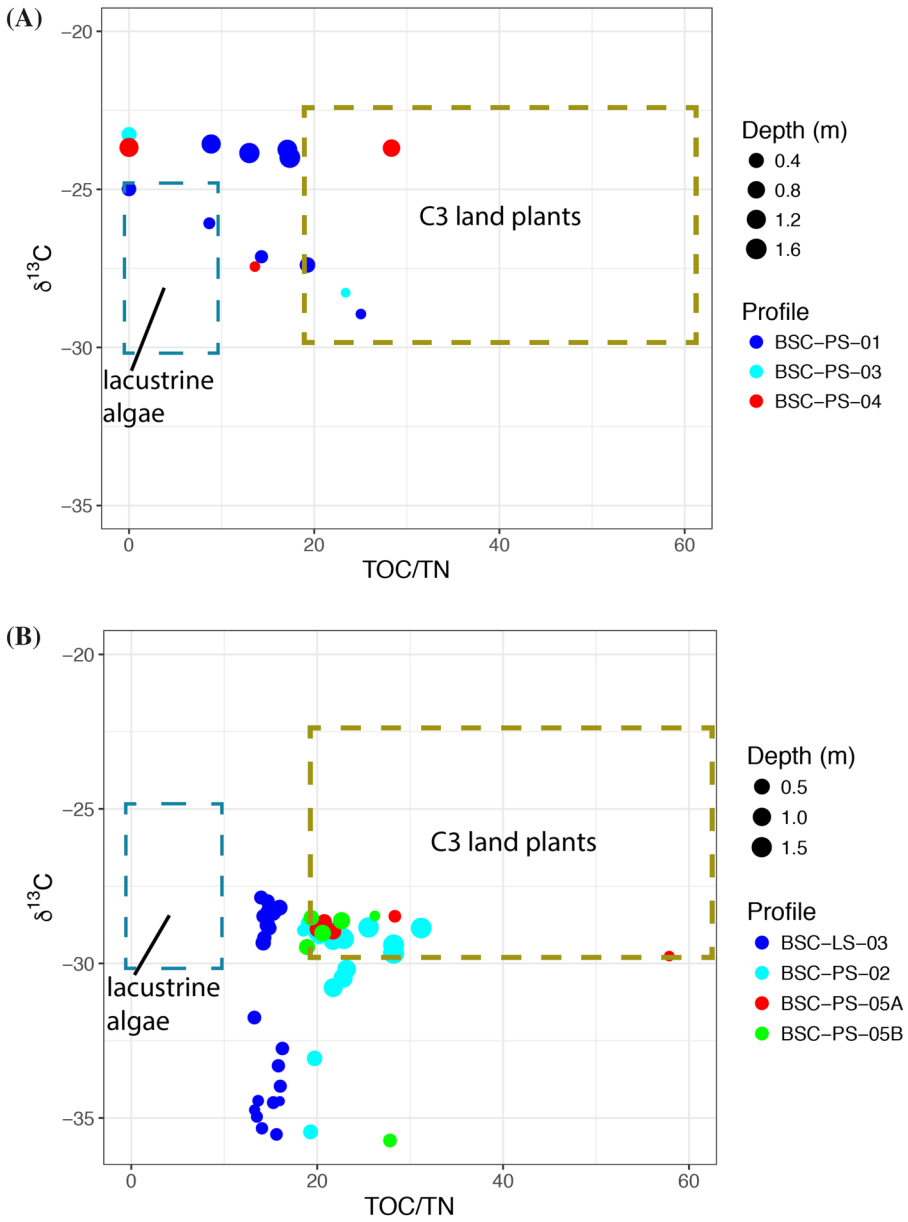

Fig. 7 TOC/TN versus $\delta^{13}C$ biplot of organic detritus analysis from (**a**) sandy soil pits BSC-PS-01, -03, -04 and from (**b**) peat sections (BSC-PS-02, -05A/B) and lake sediments (BSC-LS-03) (modified from [33])

(+0.22 to 0.00 m, Fig. 3) floating over the lake bed and which are considered living aquatic plants.

Surface water electrical conductivity, pH, and stable water isotopes

Three measurements from different depths in the Big Lake have EC values between 82 and 162 µS/cm (Table 3). The Beenchime River, for comparison, has an EC value of 79 µS/cm. For comparison, EC values from soil pit ground ice have a wider range; depending on location they can have low values of 15 to 92 µS/cm in peaty deposits near the lake (BSC-PS-05), medium values of 19 to 203 µS/cm in the peaty plateau (BSC-PS-02), or higher values of 399 to 2168 µS/cm in the sedimentary terrace (BSC-PS-01). The lake pH values range between 8.9 and 9.5. BSC-PS-01 and BSC-PS-02 have overall fairly neutral values around a pH of 7. BSC-PS-05A has an upward transition from more basic (8.5) to acidic values (5.5) (Table 3). The Beenchime River, for comparison, had a pH value of 9.2. The composition of stable isotopes from the lake water has mean values of $\delta^{18}O$ of −18.94‰ and δD of −146.54‰ (Fig. 8) and a *d*-excess between 5 and 5.1. The stable isotope composition of Beenchime River is slightly heavier with $\delta^{18}O = -17.90‰$ and $\delta D = -138.71‰$ and a *d*-excess of 4.5.

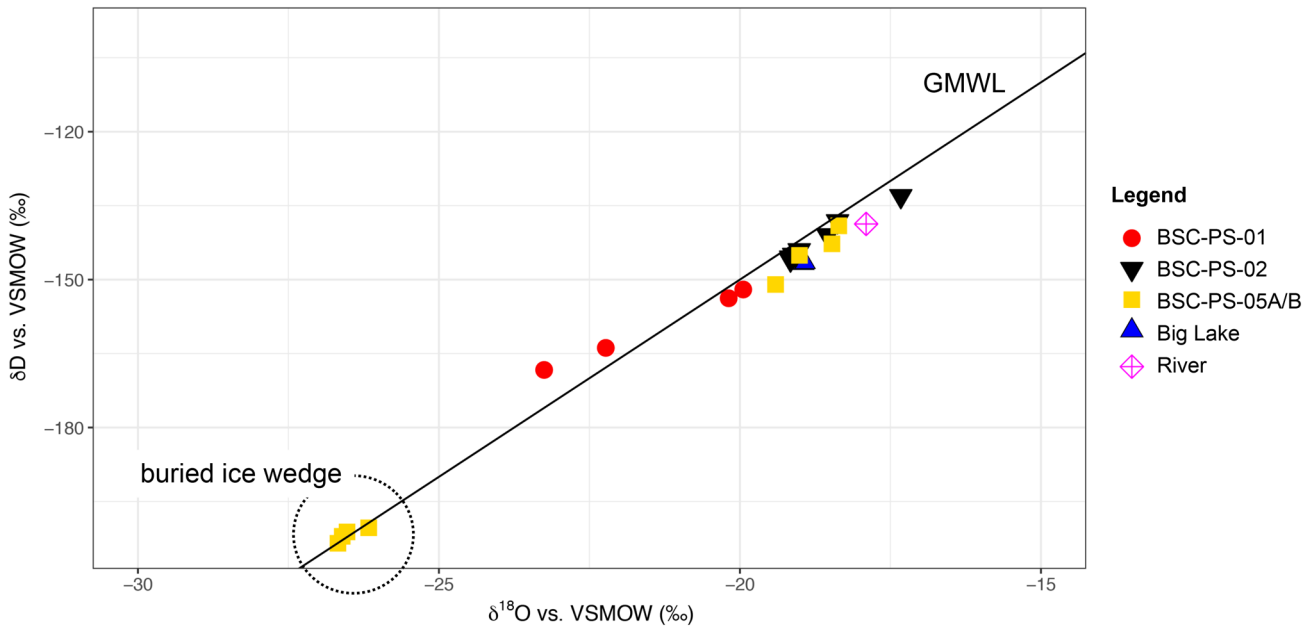

Fig. 8 δ^{18}O-δD biplot showing results from BSC water and ground ice samples. *GMWL*—global meteoric water line

Discussion of late Quaternary palaeoenvironments in the BSC

Based on dating results, we have grouped the data into two main periods; the Kargin Interstadial (50–30 cal kyr BP) and the Holocene (< 11.5 cal kyr BP) that is subdivided into the Holocene thermal optimum and the late Holocene. The discussion combines various sediment properties within one particular period.

Kargin interstadial (50–30 cal kyr BP)

Dating information is overall sparse for this time period and also includes an age reversal. The relevant sandy sections (BSC-PS-01, -03, and -04, Fig. 4a) have distinct sediment layering and partly show erosional contacts. It suggests that sediments have been relocated under different transport regimes and sediment reworking may play a role. The peak in the fine-sand spectrum remains fairly stationary in all inspected samples; only the silt portion varies to some extent (Fig. 6). We interpret that varying fluvial-to-alluvial transport energy mobilised the material along drainage pathways or as slope wash presumably during melt water periods and after rain events. The properties of detrital organic components scatter in terms of δ^{13}C and TOC/TN composition and suggest that biomass remains in the sediments stem from both, lacustrine and soil-related sources (Fig. 7). If the material is not re-worked, this would either argue for wet soil conditions in ice-wedge polygonal ponds providing a habitat to algae growth (lacustrine algae samples), or in the other case eroded fragments from land plants that have been incorporated into the sandy sediments (C3 land plants samples). This mixture from lacustrine and terrestrial detrital material is also known from other thermokarst terrain or polygonal ground in Northern Siberia [20, 45, 55].

Heavy mineral assemblages of BSC's late Quaternary detritus have pronounced occurrence of garnet, epidote, or zoisite. These minerals are likely connected to the Amphibolite or Greenschist Facies, which result from moderate pressure and temperature metamorphosis (e.g., [61]). Since bedrock around BSC is formed by Paleozoic sedimentary rock, these mineral signals may point to the Pre-Cambrian terrane orogeny of the eastern (active) margin of the Siberian Craton, where acid volcanics and carbonaceous silicites have been transformed to greenschist metamorphics and subsequently have been intruded by granites [44].

According to palaeoenvironmental reconstructions for NE Siberia, summer climates varied spatially during the Kargin Interstadial. Warm periods—when summer climates were probably as warm or nearly as warm as those at present—are determined between 39–33 cal kyr BP and 30–26 cal kyr BP [1]. This also includes a phase of thermokarst activity with thermokarst lake (alas) development. The climatic optimum of the Kargin Interstadial in the Laptev Sea region is placed between 40 and 32 cal kyr BP based on various bioindicators [2]. In this interval, it is likely that sediment mobility was increased under varying stream power especially during meltwater and summer seasons when compared with cooler periods. A lake record from the Verkhoyansk Mountains (Lake Billyakh) demonstrates that the Kargin Interstadial in

Central Yakutia was comparably wet with high lake levels and increased sedimentation rates [12]. Similar results are known from Lake Kyutunda on the western Lena side [7].

There are no dates available from the BSC for the period 33–14.5 kyear BP (~MIS 2). This might be due to the fact that the relevant deposits have been overlooked in the field, or they have been removed by subsequent erosion during MIS 1, or they are simply absent in the basin. Finally, a lack of dates and datable material may also explain this large temporal gap in the sedimentary record. By now, this issue must be left open. Sedimentation rates generally are expected to be low during the last glacial maximum (LGM), because the LGM is commonly known as being arid in the region. This is known from both, summer and winter proxy data; i.e., pollen records from lake sediments [37, 57] and ground ice stable isotopes from ice wedge formations [38].

Holocene thermal optimum (9000–6800 cal yr BP)

Lake sediment ages belong to the late early to mid-Holocene (Fig. 4b). The age distribution suggests that the time of deposition was confined to only about 1500 years between 7600 and 6100 cal yr BP with no detrital sedimentation after about 6000 cal yr BP. However, it must be noted that deeper coring may extend the datable lake sediment record though. There is one age inversion occurring, which indicates that older drift material has admixed into a sediment layer at 0.40–0.42 m depth (Table 1).

The GPR-based bathymetry shows a stepwise plunging of the slopes into the lake basin and a bumpy lake bed in the lake centre. The shape of the lake bed resembles those, which evolve from thermokarst dynamics, where ice-rich permafrost thaws out and where the depression is subsequently filled with water. Similar lakes following a thermokarst basin evolution have been described elsewhere [5–7, 17].

There is a lack of deeper reflectors in the GPR profiles, which suggests that the thickness of lake sediments amounts only to a few decimetres, unless the GPR penetration suffers from the attenuation of the electromagnetic waves. In this case, the bottom of BSC-LS-03 is seen nearly as the lake sediment bottom and it would date the onset of lake sediment deposition around 7600 cal yr BP. Deeper coring may yield a greater ages for the onset of lake formation though. Nevertheless, this time frame is similar to other thermokarst lakes found in Northern Siberia, for example Lake Nikolay in the Lena Delta, which started to form at a 7900 cal yr BP [51].

A distinct change in grain-size distributions occurs at 0.40 m core depth where overlying sediments have mean grain sizes finer for about 10 µm in the medium to fine silt fraction (Fig. 6). According to the age distribution the coarser layers at the bottom are deposited around 7600 to 7500 cal yr BP, whereas the overlying finer portion has been deposited between 7500 and 6100 cal yr BP. This argues for a loss of transportation energy into the basin after about 6100 cal yr BP. Shorelines may have retreated since then and the area, where site BSC-PS-05 has been sampled, emerged to become subaerial. Greatest age for the emerged ancient shore is 3000 cal yr BP at 0.8 m depth (Fig. 5), but might be extended with deeper coring. A regional cooling trend during the late Holocene is known from other sites in the area; a decrease of temperatures by about ~ 2 °C from warmer-than-present mid-Holocene summer temperatures until the establishment of modern conditions around 3000 years ago is reconstructed based on a regional pollen-climate transfer function [24, 25]. In BSC, this might be reflected in a shrinking lake area as is also suggested by satellite image interpretation (Fig. 6). Other reasons such as decreased precipitation and site-specific geomorphic change (i.e., changing run-off pathways) still may also play a role.

When combining the interpretations of age (mid-Holocene) and origin (thermokarst induced subaquatic morphology), the lake history matches those from e.g., Lake Nikolay [3], or Lake Kyutyunda [7], or other lakes described in Biskaborn et al. [6] and Klemm et al. [24]. Increased thermokarst activity leading to lake formation during this time is known also from the southern Laptev Sea margin (e.g., [3]). Thermokarst basins developed after the increased warming during the regional early Holocene thermal maximum [21], when summer air temperatures in Northern Yakutia were ≤ 4 °C higher than present, and precipitation was higher than present [2].

Late Holocene

Other ages acquired from soil pit sampling belong to the late Holocene (< 5000 cal yr BP) (Fig. 4a). When encountered in one section, a clear boundary between late Pleistocene and overlying late Holocene layers is not obvious though (e.g., BSC-PS-01); either because of the limited temporal resolution within the stratigraphy, or because of the absence of well-defined contrasts in measured sediment properties (Fig. 5). Grain-size compositions do not differ markedly from late Pleistocene deposits and, thus, similar transport processes are interpreted; namely snowmelt run-off and slope wash from rain events. In contrast to the late Pleistocene layers, the Holocene layers at least partly contain detrital organic components with lighter $\delta^{13}C$ values, namely in BSC-PS-02 at 0.30 m depth (i.e., < 27). Light $\delta^{13}C$ values have been found indicative for Holocene lake sediments or for Holocene peat deposits elsewhere in Northern Siberia (e.g., [52, 58]). Warmer-than-modern summer air temperatures in NE Siberia are reconstructed for the period between 3700 and 3300 cal yr BP as inferred from high values of *Betula nana* in pollen records and the continuance of Larix

north of its present range [4]. In BSC especially peat (BSC-PS-02) and other organic-rich sediments (BSC-PS-05) are formed during this time. The organogenic deposits accumulated in boggy lowland and along water-logged drainage pathways and their accumulation areas are shaped by polygonal ice wedge growth. The peat formation period during late Holocene time is similar as described from other sites in Siberia north of the treeline [41]. Hereafter (< 3300 cal yr BP), environmental conditions are reconstructed to be similar to those at present [2].

Ground ice samples taken from sand and peat sections plot relatively well on the GMWL, which suggests a low impact of secondary evaporation or refreezing on its formation (Fig. 8). Only two samples from BSC-PS-01 are found above the GMWL indicative for a more evaporated vapour source (e.g., [42]). EC in one of these two samples (sample depth 1.40–1.60 m) peaks at 2168 µS/cm (Table 3). Possibly, this EC peak evolved from an active layer thawing and refreezing deeper than modern, where two freezing fronts from below and above have caused an enrichment of the light soluble fraction between the fronts before final refreezing. This refreezing process might also have caused the depletion of stable water isotopes along the freezing front in the same part of the section. Similar freezing front dynamics have been observed elsewhere [16]. The deeper than modern active layer dynamics might be related to local factors or to palaeoclimate events such as the Holocene thermal optimum in the area (see [31]).

The stable isotope composition with $\delta^{18}O$ values around −18‰ for many of the samples is interpreted to result from syngenetic freezing during late Holocene time. The stable isotopes from the intrasedimental ground ice (mixture from rain and snow, [53] is clearly heavier than few individual samples related to buried ice wedge ice, which has been hit at the bottom of section BSC-PS-05 (Fig. 8). Here, close to the lake shore ice-wedge polygons have developed in organic-rich sediments. Whereas intrasedimental ground ice results from a mixture of snowmelt and rain [53], massive ground ice, including ice wedges, is fed by snowmelt only and has a lighter stable isotope composition. Values of massive ground ice in BSC-PS-05 match those described for the Holocene from Northern Siberia [46, 48] or are lighter than those described for Holocene samples from the Lena Delta region [32], but ice wedge formation in BSC may take place under more continental climate conditions in the Yakutian hinterland than those placed around the Laptev Sea margin. Nevertheless, $\delta^{18}O$ values around −26 ‰ from BSC ice wedges are similar to those described from late Holocene ice wedges sampled at the Batagay mega slump; whereby the Batagay site at the lower reaches of the Yana River has a more continental setting with $\delta^{18}O$ values for late Holocene ice wedges of −29 ‰ [38].

The core portion above the massive ground ice (< 0.7 m depth) shows a similar isotopic signature like lake water. Presumably, the same source, a mixture of snowmelt and rain, is assumed to feed the lake and temporarily infiltrated the shore lines during Holocene time.

Water isotope signatures of the three Big Lake samples from different water depths (Fig. 8) reveal a well-mixed summer water body with similar isotopic composition and *d*-excess. A *d*-excess around 5‰ indicates an evaporative character of the lake system [22]. For comparison, the isotopic ratio of the river water is ~ 7.5‰ higher for δD and ~ 1‰ higher for $\delta^{18}O$ with a lower *d*-excess (~ 0.5‰ lower). This difference suggests a higher input from snowmelt to the lake when compared with the river water.

Conclusions

The BSC basin is partly covered by fluvial/alluvial sediments from the MIS 3 and the late MIS 1 periods and from lake sediments that have been deposited between 7600 and 6100 cal yr BP. The late Quaternary sedimentation history is summarised in three stages:

(i) the mobilisation of fluvial/alluvial sediments along the lowland drainage pattern between 50 and 30 cal kyear BP;
(ii) a thermokarst lake formation during the Holocene thermal maximum (between 7600 and 6100 cal yr BP), a first shrinkage of the thermokarst lake (Big Lake) after 7500 cal yr BP (expressed in a grain-size shift), and a second shrinkage after 6100 cal yr BP (absence of detrital sedimentation after 6100 cal yr BP);
(iii) a re-mobilisation of fluvial/alluvial sediments along the lowland drainage pattern, an accumulation of peaty and organic-rich sediments, and the formation of ice-wedge polygons between 5700 and 1500 cal yr BP.

The sedimentation during the late Quaternary in BSC likely results from weathering and erosion of the underlying Palaeozoic bedrock. The thickness of Quaternary deposits has yet to be defined. This requires deeper geophysical investigations and deeper drilling. The basin nowadays acts as an intermediate sediment storage place before the detrital sediments are exported to the west and south where the crater rim is eroded.

Acknowledgements Open Access funding provided by Projekt DEAL. We highly acknowledge the partial project funding through the International Office (IB) of BMBF (German Ministry for Science and Research, Grant No. 01DJ15027). Logistical help was given in the

frame of the German-Russian Expedition "Lena 2016" including services by the Hydrobase Tiksi. Ingmar Nitze kindly provided satellite imagery.

Compliance with ethical standards

Conflict of interest There is no conflict of interest.

References

1. Anderson PM, Lozhkin AV (2001) The stage 3 interstadial complex (Karginskii/middle Wisconsinan interval) of Beringia: variations in paleoenvironments and implications for paleoclimatic interpretations. Quatern Sci Rev 20:93–125. https://doi.org/10.1016/S0277-3791(00)00129-3
2. Andreev AA, Schirrmeister L, Tarasov PE, Ganopolski A, Brovkin V, Siegert C, Wetterich S, Hubberten H-W (2011) Vegetation and climate history in the Laptev Sea region (Arctic Siberia) during Late Quaternary inferred from pollen records. Quatern Sci Rev 30:2182–2199. https://doi.org/10.1016/j.quascirev.2010.12.026
3. Andreev A, Tarasov P, Schwamborn G, Ilyashuk B, Ilyashuk E, Bobrov A, Klimanov V, Rachold V, Hubberten HW (2004) Holocene paleoenvironmental records from Nikolay Lake, Lena River Delta, Arctic Russia. Palaeogeogr Palaeoclimatol Palaeoecol 209:197–217. https://doi.org/10.1016/j.palaeo.2004.02.010
4. Binney HA, Willis KJ, Edwards ME, Bhagwat SA, Anderson PM, Andreev AA, Blaauw M, Damblon F, Haesaerts P, Kienast F, Kremenetski KV, Krivonogov SK, Lozhkin AV, MacDonald GM, Novenko PO, Sapelko T, Väliranta M, Vazhenina L (2009) The distribution of late-Quaternary woody taxa in northern Eurasia: evidence from a new macrofossil database. Quatern Sci Rev 28:2445–2464. https://doi.org/10.1016/j.quascirev.2009.04.016
5. Biskaborn BK, Herzschuh U, Bolshiyanov DY, Schwamborn G, Diekmann B (2013a) Thermokarst processes and depositional events in a tundra lake, northeastern Siberia. Permafrost Periglac Process 24:160–174
6. Biskaborn BK, Herzschuh U, Bolshiyanov D, Savelieva L, Zibulski R, Diekmann B (2013b) Late Holocene thermokarst variability inferred from diatoms in a lake sediment record from the Lena Delta, Siberian Arctic. J Paleolimnol 49:155–170. https://doi.org/10.1007/s10933-012-9650-1
7. Biskaborn BK, Subetto DA, Savelieva LA, Vakhrameeva PS, Hansche A, Herzschuh U et al (2016) Late Quaternary vegetation and lake system dynamics in north-eastern Siberia: implications for seasonal climate variability. Quatern Sci Rev 147:406–421. https://doi.org/10.1016/j.quascirev.2015.08.014
8. Biskaborn BK, Smith SL, Noetzli J, Matthes H, Vieira G, Streletskiy DA, Schoeneich P, Romanovsky VE, Lewkowicz AG, Abramov A, Allard M, Boike J, Cable WL, Christiansen HH, Delaloye R, Diekmann B, Drozdov D, Etzelmüller B, Grosse G, Guglielmin M, Ingeman-Nielsen T, Isaksen K, Ishikawa M, Johansson M, Johannsson H, Joo A, Kaverin D, Kholodov A, Konstantinov P, Kröger T, Lambiel C, Lanckman JP, Luo D, Malkova G, Meiklejohn I, Moskalenko N, Oliva M, Phillips M, Ramos M, Sannel ABK, Sergeev D, Seybold C, Skryabin P, Vasiliev A, Wu Q, Yoshikawa K, Zheleznyak M, Lantuit H (2019) Permafrost is warming at a global scale. Nat Commun 10:264. https://doi.org/10.1038/s41467-018-08240-4
9. Boenigk W (1983) Schwermineralanalyse. Enke Stuttgart. p. 152
10. Brigham-Grette J, Melles M, Minyuk P, Andreev A, Tarasov P, DeConto R, Koenig S, Nowaczyk N, Wennrich V, Rosén P, Haltia-Hovi E, Cook T, Gebhardt C, Meyer-Jacob C, Snyder J, Herzschuh U (2013) Pliocene warmth, extreme polar amplification, and stepped Pleistocene cooling recorded in NE Russia. Science 340:1421–1427
11. Dansgaard W (1963) Stable isotopes in precipitation. Tellus 16:436–468. https://doi.org/10.1111/j.2153-3490.1964.tb00181.x
12. Diekmann B, Pestryakova L, Nazarova L, Subetto D, Tarasov PE, Stauch G et al (2017) Late Quaternary lake dynamics in the Verkhoyansk Mountains of Eastern Siberia: implications for climate and glaciation history. Polarforschung 86(2):97–110. https://doi.org/10.2312/polarforschung.86.2.97
13. Duchkov AD, Zheleznjak M, Sokolova LS (2014) Electronic geothermal atlases of Asian Russia. Sci Cold Arid Reg 6:479–483. https://doi.org/10.3724/SP.J.1226.2014.00479
14. EarthImpactDatabase (2019) https://www.passc.net/EarthImpactDatabase/New%2520website_05-2018/AsiaRussia.html. Nov 2019
15. Ehlers J, Gibbard PL (2007) The extent and chronology of Cenozoic global glaciation. Quatern Int 164:6–20. https://doi.org/10.1016/j.quaint.2006.10.008
16. Fritz M, Wetterich S, Meyer H, Schirrmeister L, Lantuit H, Pollard WH (2011) Origin and characteristics of massive ground ice on Herschel Island (Western Canadian Arctic) as revealed by stable water isotope and hydrochemical signatures. Permafrost Periglac Process 22:26–38. https://doi.org/10.1002/ppp.714
17. Gasperini L, Alvisi F, Biasini G, Bonatti E, Longo G, Pipan M et al (2007) A possible impact crater for the 1908 Tunguska Event. Terra Nova 19:245–251. https://doi.org/10.1111/j.1365-3121.2007.00742.x
18. Grieve RA (1987) Terrestrial impact structures. Annu Rev Earth Planet Sci 15:245–270
19. Hubberten HW, Andreev A, Astakhov VI, Demidov I, Dowdeswell JA, Henriksen M, Hjort C, Houmark-Nielsen M, Jakobsson M, Kuzmina S et al (2004) The periglacial climate and environment in northern Eurasia during the Last Glaciation. Quatern Sci Rev 23:1333–1357. https://doi.org/10.1016/j.quascirev.2003.12.012
20. Jongejans LL, Strauss J, Lenz J, Peterse F, Mangelsdorf K, Fuchs M, Grosse G (2018) Organic matter characteristics in Yedoma and thermokarst deposits on Baldwin Peninsula, west Alaska. Biogeosciences 15:6033–6048. https://doi.org/10.5194/bg-15-6033-2018
21. Kaufman DS, Ager TA, Anderson NJ, Anderson PM, Andrews JT, Bartlein PJ et al (2004) Holocene thermal maximum in the western Arctic (0–180 W). Quatern Sci Rev 23:529–560. https://doi.org/10.1016/j.quascirev.2003.09.007
22. Kendall C, Caldwell EA (1998) Fundamentals of isotope geochemistry. In: Kendall C, McDonnell JJ (eds) Isotope tracers in catchment hydrology, 1st edn. Elsevier, Amsterdam, pp 51–86
23. Khain VE (1985) Geology of the USSR/Geology of Northern Eurasia (Ex-USSR). Beiträge zur regionalen Geologie der Erde; 24 Geology of the USSR; Part 2. Borntraeger, Berlin
24. Klemm J, Herzschuh U, Pestryakova LA (2016) Vegetation, climate and lake changes over the last 7000 years at the boreal

treeline in north-central Siberia. Quatern Sci Rev 147:422–434. https://doi.org/10.1016/j.quascirev.2015.08.015
25. Klemm J, Herzschuh U, Pisaric MF, Telford RJ, Heim B, Pestryakova LA (2013) A pollen-climate transfer function from the tundra and taiga vegetation in Arctic Siberia and its applicability to a Holocene record. Palaeogeogr Palaeoclimatol Palaeoecol 386:702–713. https://doi.org/10.1016/j.palaeo.2013.06.033
26. Kosygin YA, Parfenov L (1975) Structural evolution of eastern Siberia and adjacent areas. Am J Sci 275:187–208
27. Lunardini VJ (1995) Permafrost formation time. Cold Regions Research and Engineering Lab. Report 95-8, US Army Corps of Engineers, Lab Hanover, p 44. https://apps.dtic.mil/sti/pdfs/ADA295515.pdf. Accessed May 2020
28. Mange MA, Maurer HFW (1991) Schwerminerale in Farbe, Stuttgart (Enke), p. 148
29. Masaitis V (1999) Impact structures of northeastern Eurasia: the territories of Russia and adjacent countries. Meteorit Planet Sci 34:691–711. https://doi.org/10.1111/j.1945-5100.1999.tb01381.x
30. Melles M, Brigham-Grette J, Minyuk PS, Nowaczyk NR, Wennrich V, DeConto RM, Haltia-Hovi E (2012) 2.8 Million years of Arctic climate change from Lake El'gygytgyn, NE Russia. Science 337(6092):315–320. https://doi.org/10.1126/science.1222135
31. Meyer H, Dereviagin A, Siegert C, Schirrmeister L, Hubberten HW (2002) Palaeoclimate reconstruction on Big Lyakhovsky Island, north Siberia: hydrogen and oxygen isotopes in ice wedges. Permafrost Periglac Process 13:91–105. https://doi.org/10.1002/ppp.416
32. Meyer H, Opel T, Laepple T, Dereviagin AY, Hoffmann K, Werner M (2015) Long-term winter warming trend in the Siberian Arctic during the mid-to late Holocene. Nat Geosci 8:122–125. https://doi.org/10.1038/NGEO2349
33. Meyers PA (1994) Preservation of elemental and isotopic source identification of sedimentary organic matter. Chem Geol 114(3–4):289–302
34. Mikhailov M, Shurygin A, Kharyuzov L (1978) The Beyenchime Salaata meteorite crater. Doklady Akademii Nauk SSSR 245:76–78 **(in Russian)**
35. Moon HK, Mi BH, Fletcher AB, Kim BG (2001) Terrestrial impact cratering chronology: a preliminary analysis. J Astron Space Sci 18:191–208
36. Moran K, Backman J, Brinkhuis H, Clemens SC, Cronin T, Dickens GR et al (2006) The Cenozoic palaeoenvironment of the Arctic Ocean. Nature 441(7093):601–605. https://doi.org/10.1038/nature04800
37. Müller S, Tarasov PE, Andreev AA, Tütken T, Gartz S, Diekmann B (2010) Late Quaternary vegetation and environments in the Verkhoyansk Mountains region (NE Asia) reconstructed from a 50-kyr fossil pollen record from Lake Billyakh. Quatern Sci Rev 29:2071–2086. https://doi.org/10.1016/j.quascirev.2010.04.024
38. Opel T, Murton JB, Wetterich S, Meyer H, Ashastina K, Günther F, Grotheer H, Mollenhauer G, Danilov PP, Boeskorov V, Savvinov GN, Schirrmeister L (2019) Past climate and continentality inferred from ice wedges at Batagay megaslump in the Northern Hemisphere's most continental region, Yana Highlands, interior Yakutia. Clim Past 15:1443–1461. https://doi.org/10.5194/cp-15-1443-2019
39. Ostashkin I, Kareva EV, Marchenko NK (1990) Geological interpretation of air photography and cosmic photography materials with additional inspection works for search meaningful interpreted structures and draw geological map with scale 1:200000 in the area between river Bur and Olenek (in Russian)
40. PlanetScope (2020) Planet Team, Planet application program interface. In: Space for life on earth. San Francisco, CA. https://api.planet.com
41. Peteet D, Andreev A, Bardeen W, Mistretta F (1998) Long-term Arctic peatland dynamics, vegetation and climate history of the Pur-Taz region, Western Siberia. Boreas 27:115–126. https://doi.org/10.1111/j.1502-3885.1998.tb00872.x
42. Petermann E, Gibson JJ, Knoller K, Pannier T, Weiss H, Schubert M (2018) Determination of groundwater exchange rates and water residence time of groundwater-fed lakes based on stable isotopes of water (^{18}O, ^{2}H) and radon (^{222}Rn) mass balances. Hydrol Process 32(6):805–816. https://doi.org/10.1002/hyp.11456
43. Pinchuk L (1971) Morphology and genesis of the Beenchime-Salaatinsky depression—Kimberlite volcanism and prospects of primary diamond content of the north-eastern Siberian platform. In: Proceedings Arctic Geology Research Institute, Leningrad pp.123–126 (in Russian)
44. Rosen OM (2002) Siberian craton—a fragment of a Paleoproterozoic supercontinent. Russ J Earth Sci 4(2):103–119
45. Schirrmeister L, Grosse G, Wetterich S, Overduin PP, Strauss J, Schuur EAG, Hubberten H-W (2011) Fossil organic matter characteristics in permafrost deposits of the northeast Siberian Arctic. J Geophys Res Biogeo 116:1–16. https://doi.org/10.1029/2011JG001647
46. Schirrmeister L, Siegert C, Kuznetsova T, Kuzmina S, Andreev A, Kienast F, Meyer H, Bobrov A (2002) Paleoenvironmental and paleoclimatic records from permafrost deposits in the Arctic region of northern Siberia. Quatern Int 89:97–118. https://doi.org/10.1016/S1040-6182(01)00083-0
47. Schirrmeister L, Froese D, Tumskoy V, Grosse G, Wetterich S (2013) Yedoma: late Pleistocene ice-rich syngenetic permafrost of Beringia. In: Encyclopedia of Quaternary Science. 2nd edn, pp 542–552
48. Schirrmeister L, Bobrov A, Raschke E, Herzschuh U, Strauss J, Pestryakova LA, Wetterich S (2018) Late Holocene ice-wedge polygon dynamics in northeastern Siberian coastal lowlands. Arct Antarct Alp Res 50(1):e1462595. https://doi.org/10.1080/15230430.2018.1462595
49. Schirrmeister L, Dietze E, Matthes H, Grosse G, Strauss J, Laboor S, Ulrich M, Kienast F, Wetterich S (2020) The genesis of Yedoma Ice Complex permafrost—grain-size endmember modeling analysis from Siberia and Alaska. E&G Quatern Sci J 69:33–53. https://doi.org/10.5194/egqsj-69-33-2020
50. Schwamborn G, Schirrmeister L, Manthey C, Raschke U, Zhuravlev A, Oparin N, Oshchepkova M, Prokopiev A (2017) 4. Beenchime, 4.1. Reconnaissance study at Beenchime Salaatinsky Crater. In: Overduin P, Blender F, Bolshiyanov D, Grigoriev M, Morgenstern A, Meyer H (eds) Russian–German cooperation: expeditions to Siberia in 2016. In Berichte zur Polar- und Meeresforschung. Reports on polar and marine research, Bremerhaven, Alfred Wegener Institute for Polar and Marine Research 709:108–129. doi: 10.2312/BzPM_0709_2017s
51. Schwamborn GJ, Dix JK, Bull JM, Rachold V (2002a) High-resolution seismic and ground penetrating radar-geophysical profiling of a thermokarst lake in the western Lena Delta, Northern Siberia. Permafrost Periglac Process 13:259–269
52. Schwamborn G, Andreev A, Rachold V, Hubberten H-W, Grigoriev MN, Tumskoy V, Pavlova EY, Dorozkhina MV (2002b) Evolution of Lake Nikolay, Arga Island, Western Lena River delta, during Late Pleistocene and Holocene time. Polarforschung 70:69–82
53. Schwamborn G, Meyer H, Fedorov G, Schirrmeister L, Hubberten H-W (2006) Ground ice and slope sediments archiving late Quaternary paleoenvironment and paleoclimate signals at the margins of El'gygytgyn Impact Crater, NE Siberia. Quatern Res 66:259–272. https://doi.org/10.1016/j.yqres.2006.06.007
54. Strauss J, Schirrmeister L, Grosse G, Fortier D, Hugelius G, Knoblauch C, Romanovsky V, Schädel C, Schneider von Deimling T, Schuur EAG, Shmelev D, Ulrich M, Veremeeva A (2017) Deep

Yedoma permafrost: a synthesis of depositional characteristics and carbon vulnerability. Earth Sci Rev 172:75–86. https://doi.org/10.1016/j.earscirev.2017.07.007
55. Strauss J, Schirrmeister L, Mangelsdorf K, Eichhorn L, Wetterich S, Herzschuh U (2015) Organic-matter quality of deep permafrost carbon—a study from Arctic Siberia. Biogeosciences 12(7):2227–2245. https://doi.org/10.5194/bg-12-2227-2015
56. Stuiver M, Reimer PJ, Reimer RW (2019) CALIB 7.1 [WWW program] at https://calib.org. Accessed 12 Feb 2019
57. Tarasov PE, Müller S, Zech M, Andreeva D, Diekmann B, Leipe C (2013) Last glacial vegetation reconstructions in the extreme-continental eastern Asia: potentials of pollen and *n*-alkane biomarker analyses. Quatern Int 290:253–263. https://doi.org/10.1016/j.quaint.2012.04.007
58. Wetterich S, Kuzmina S, Andreev AA, Kienast F, Meyer H, Schirrmeister L, Kuznetsova T, Sierralta M (2008) Palaeoenvironmental dynamics inferred from late Quaternary permafrost deposits on Kurungnakh Island, Lena Delta, northeast Siberia, Russia. Quatern Sci Rev 27:1523–1540. https://doi.org/10.1016/j.quascirev.2008.04.007
59. Wetterich S, Rudaya N, Tumskoy V, Andreev AA, Opel T, Schirrmeister L, Meyer H (2011) Last glacial maximum records in permafrost of the East Siberian Arctic. Quatern Sci Rev 30:3139–3151. https://doi.org/10.1016/j.quascirev.2011.07.020
60. Wetterich S, Rudaya N, Kuznetsov V, Maksimov F, Opel T, Meyer H et al (2019) Ice Complex formation on Bol'shoy Lyakhovsky Island (New Siberian Archipelago, East Siberian Arctic) since about 200 ka. Quatern Res 92:530–548. https://doi.org/10.1017/qua.2019.6
61. Winter JD (2001) An introduction to igneous and metamorphic petrology, vol 697. Prentice Hall, New Jersey, p 697